

Conditional Diffusion Model-Enabled Scenario-Specific Neural Receivers for Superimposed Pilot Schemes

Xingyu Zhou, Le Liang, Xinjie Li, Jing Zhang,
Peiwen Jiang, Xiao Li, and Shi Jin

Abstract

Neural receivers have demonstrated strong performance in wireless communication systems. However, their effectiveness typically depends on access to large-scale, scenario-specific channel data for training, which is often difficult to obtain in practice. Recently, generative artificial intelligence (AI) models, particularly diffusion models (DMs), have emerged as effective tools for synthesizing high-dimensional data. This paper presents a scenario-specific channel generation method based on conditional DMs, which accurately model channel distributions conditioned on user location and velocity information. The generated synthetic channel data are then employed for data augmentation to improve the training of a neural receiver designed for superimposed pilot-based transmission. Experimental results show that the proposed method generates high-fidelity channel samples and significantly enhances neural receiver performance in the target scenarios, outperforming conventional data augmentation and generative adversarial network-based techniques.

Index Terms

Deep learning, generative AI, diffusion models, data augmentation, superimposed pilots

I. INTRODUCTION

Channel state information (CSI) is essential for fully exploiting the benefits of multiple-input multiple-output (MIMO) technology in wireless communication systems. However, acquiring

Xingyu Zhou, Le Liang, Xinjie Li, Jing Zhang, Peiwen Jiang, Xiao Li, and Shi Jin are with the School of Information Science and Engineering, Southeast University, Nanjing 210096, China (e-mail: xy_zhou@seu.edu.cn; lliang@seu.edu.cn; lixinjie@seu.edu.cn; jingzhang@seu.edu.cn; peiwenjiang@seu.edu.cn; li_xiao@seu.edu.cn; jinshi@seu.edu.cn). Le Liang is also with Purple Mountain Laboratories, Nanjing 211111, China. (*Corresponding author: Shi Jin; Le Liang.*)

accurate CSI typically requires a large number of pilot symbols, which are time-multiplexed with data symbols and result in substantial transmission overhead. To improve spectral efficiency, superimposed pilot (SIP) schemes have attracted increasing interest [1]–[3]. In these schemes, pilot symbols are embedded within data symbols instead of being allocated to dedicated time-frequency resources, as in conventional orthogonal pilot (OP) transmission. While SIP schemes reduce pilot overhead, especially in high-mobility environments, they introduce challenges such as mutual interference between pilot and data symbols, which complicates channel estimation and symbol detection tasks [4].

In recent years, artificial intelligence (AI) and deep learning (DL) have shown great potential in solving problems that are difficult to address through conventional wireless system design approaches [5]. In particular, neural receivers, DL-based architectures that learn to demodulate signals directly from raw input data, have emerged as promising solutions for overcoming the limitations of SIP schemes. Their ability to capture nonlinear relationships and adapt to dynamic channel conditions makes them especially useful in such settings [6]–[9]. However, the effectiveness of neural receivers heavily depends on the availability of large-scale, diverse training datasets that accurately reflect realistic channel conditions. Acquiring such datasets remains a significant challenge due to limitations in channel measurement, storage, and computational resources [10]. This issue is further exacerbated as wireless systems evolve toward ultra-massive MIMO architectures, which involve extremely high-dimensional channel representations [11]. Additionally, channel characteristics vary rapidly across different environments, making it difficult for neural receivers to generalize effectively. The scenario-adaptability of these models therefore remains a critical challenge. This has motivated growing interest in data augmentation techniques, which aim to synthetically enrich training datasets and improve the robustness and generalization capability of neural receivers.

Recent developments in generative AI have introduced transformative opportunities in wireless communications [12]. Deep generative models have been successfully applied in tasks such as channel modeling [13], [14], channel estimation [15], [16], and data augmentation for downstream learning tasks [17], [18]. Among these models, diffusion models (DMs) [19]–[21] have demonstrated exceptional performance in generating high-fidelity data and capturing complex data distributions. Despite their potential, the use of DMs for scenario-specific data generation and augmentation in learning-based communication systems remains relatively unexplored. In particular, their ability to support neural receiver training through environment-aware synthetic

channel generation has not been fully investigated.

A key advantage of DMs lies in their ability to generate conditional data distributions, making them suitable for capturing the relationships between environmental contexts, such as user location and mobility, and channel behavior. This conditional generation capability enables tailored, scenario-specific data synthesis. A prior study [10] proposed a DM-based approach to generate channel samples based on user equipment (UE) location. However, this method did not account for the coexistence of diverse environmental conditions within a typical urban cell [22], and it lacked mechanisms for enhancing neural receiver performance in specific scenarios.

In this paper, we develop a DM-based channel data generation framework aimed at scenario-specific augmentation of neural receivers in SIP-based transmissions. By conditioning the model on environmental inputs, including UE location and speed, the proposed DM effectively captures key channel features such as angular, delay, and temporal characteristics. The model is trained using a limited amount of high-fidelity channel data generated from simulation tools. A consistency distillation strategy is further incorporated to significantly reduce the generation complexity and latency, enabling practical deployment. The synthetic channel samples closely match the true distribution of the target scenario and are used to construct an augmented training dataset for the neural receiver. Simulation results show that the proposed approach significantly improves the performance of neural receivers under SIP schemes, outperforming conventional data augmentation techniques and generative adversarial network (GAN)-based methods. Its performance approaches that achieved by models trained with abundant true channel data.

The main contributions of this paper are summarized as follows:

- **Conditional DM Framework for Scenario-Specific Channel Generation:** We introduce a DM-based framework that generates scenario-specific channel samples conditioned on UE location and speed. This method outperforms GAN-based alternatives in distributional similarity metrics and significantly enhances neural receiver performance in the targeted scenarios.
- **Dual U-Net Architecture for 3D CSI Feature Learning:** A specialized DM architecture is developed using two sequential U-Nets that operate in distinct two-dimensional (2D) domains of the three-dimensional (3D) CSI, effectively learning angular, delay, and temporal characteristics of the channel.
- **Consistency Distillation for Efficient Inference:** To address the high computational cost of standard DMs, we employ a consistency distillation scheme that accelerates inference

by a factor of 80 while maintaining the fidelity of generated samples, enabling practical real-time application.

Notations: Bold uppercase and lowercase letters denote matrices and vectors, respectively. $(\cdot)^H$ is the Hermitian transpose, and \odot denotes the Hadamard product. $\mathbf{0}$ and \mathbf{I} represent the zero vector and identity matrix, while $\|\cdot\|_2$ is the l_2 norm. $\mathbb{E}[\cdot]$ denotes expectation. $\mathcal{N}(z; \mu, \sigma^2)$ and $\mathcal{U}(\mathcal{A})$ denote Gaussian and uniform distributions, respectively. \mathbb{R} and \mathbb{C} represent the sets of real and complex numbers, respectively.

II. PROBLEM FORMULATION

A. System Model

Consider a point-to-point uplink MIMO system in which the base station (BS) is equipped with N_r receive antennas, and the UE is equipped with N_t transmit antennas. Both the BS and UE employ uniform linear arrays (ULAs) with half-wavelength spacing between antenna elements. An orthogonal frequency division multiplexing (OFDM) scheme is adopted, where each frame consists of K subcarriers and S consecutive symbols, resulting in $V = KS$ time-frequency resource elements (REs). The channel is modeled using a geometric channel model. The complex-valued channel matrix for the (k, s) -th RE, denoted by $\mathbf{H}_{\text{cplx}}^{(k,s)} \in \mathbb{C}^{N_r \times N_t}$ for $k \in \{1, \dots, K\}$ and $s \in \{1, \dots, S\}$, is expressed as

$$\mathbf{H}_{\text{cplx}}^{(k,s)} = \sum_{l=1}^L \gamma_l^{(k,s)} \mathbf{a}_r(\theta_l) \mathbf{a}_t^H(\phi_l), \quad (1)$$

where L denotes the number of propagation paths, and $\gamma_l^{(k,s)}$ represents the complex gain of the l -th path at the (k, s) -th RE. The vectors $\mathbf{a}_t(\cdot)$ and $\mathbf{a}_r(\cdot)$ denote the transmit and receive array response vectors, respectively. The parameters ϕ_l and θ_l represent the azimuth angles of departure and arrival for the l -th path. By stacking $\mathbf{H}_{\text{cplx}}^{(k,s)}$ across the frequency and time dimensions, the complete channel tensor is obtained as $\mathbf{H}_{\text{cplx}} \in \mathbb{C}^{N_r \times N_t \times K \times S}$.

The UE employs SIP transmission, where the transmitted block from the n -th transmit antenna ($n \in \{1, \dots, N_t\}$) is constructed by superimposing a pilot matrix $\mathbf{P}_n \in \mathbb{C}^{K \times S}$ and a data matrix $\mathbf{D}_n \in \mathbb{C}^{K \times S}$ as follows

$$\mathbf{S}_n = \sqrt{\rho} \mathbf{P}_n + \sqrt{1 - \rho} \mathbf{D}_n, \quad (2)$$

where $\rho \in [0, 1]$ denotes the power allocation factor between pilot and data signals. The received signal at the m -th antenna of the BS, denoted as $\mathbf{Y}_m \in \mathbb{C}^{K \times S}$, can be expressed as

$$\mathbf{Y}_m = \sum_{n=1}^{N_t} \mathbf{H}_{\text{cplx},m,n} \odot \mathbf{S}_n + \mathbf{N}_m, \quad (3)$$

where $\mathbf{H}_{\text{cplx},m,n} \in \mathbb{C}^{K \times S}$ is the frequency-time domain channel matrix between the n -th transmit antenna and the m -th receive antenna, extracted as a slice from the full channel tensor \mathbf{H}_{cplx} . The matrix \mathbf{N}_m represents additive white Gaussian noise (AWGN).

The goal of the receiver is to recover the transmitted data symbols and decode the corresponding message bits. Conventional approaches typically rely on separate modules for channel estimation and symbol detection. However, SIP transmission introduces mutual interference between pilot and data components, which complicates the separation of the two signals and increases the difficulty of accurate recovery. To address this issue, the neural receiver proposed in [6] leverages data-driven neural networks (NNs) to jointly perform channel estimation and data detection, while incorporating an interference cancellation mechanism. Despite its effectiveness, this approach requires a large-scale training dataset with approximately 10^6 channel samples to achieve reliable accuracy and generalization. Such a requirement imposes considerable burdens in terms of channel measurement, data collection, and storage.

B. Channels Across Multiple Scenarios

An urban micro-cell environment typically comprises multiple scenarios with distinct characteristics [22], which are reflected in the UE's surrounding scattering conditions and mobility patterns, as illustrated in Fig. 1. These diverse scenarios result in significantly different channel distributions, which in turn influence signal propagation and receiver design.

We begin by examining the impact of the UE's surrounding scatterers, which are primarily determined by its location, assuming a fixed environmental configuration within the cell. For simplicity, the UE height is fixed, and its location is represented by two-dimensional planar coordinates $[x, y]$. Based on the geometry-based channel model in (1), the channel parameters $\gamma_l^{(k,s)}$, ϕ_l , θ_l for $l \in \{1, \dots, L\}$, as well as the number of propagation paths L , are conditionally dependent on the UE's location. This dependency implies that the statistical distribution of the wireless channel is inherently location-dependent.

To simplify the discussion, we consider a single-antenna UE ($N_t = 1$) and focus on the angular-delay domain representation of the channel, denoted as $\mathbf{H}_{\text{AD}} \in \mathbb{C}^{N_r \times \tau}$, where $\tau < K$

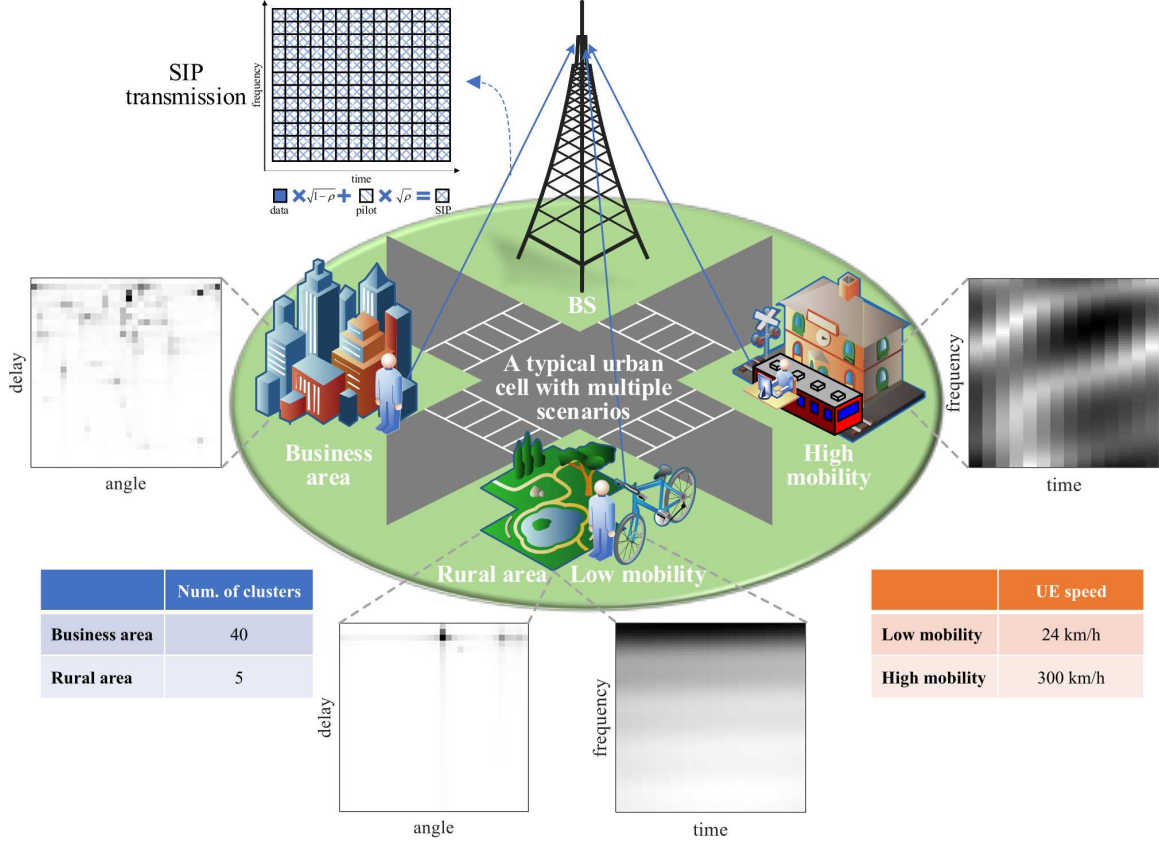


Fig. 1. A typical urban cell containing multiple scenarios, where the uplink transmission adopts the SIP scheme. The channel sample of each scenario is displayed using grayscale map.

represents the number of non-zero delay components retained in the delay domain [22]. This representation captures key characteristics such as multipath delay and angular dispersion and is obtained by applying a two-dimensional fast Fourier transform (2D-FFT) to the spatial-frequency domain channel matrix $\mathbf{H}_{\text{SF}} = [\mathbf{h}_{\text{cplx}}^{(1)}, \dots, \mathbf{h}_{\text{cplx}}^{(K)}]$, where each $\mathbf{h}_{\text{cplx}}^{(k)} \in \mathbb{C}^{N_r \times 1}$ denotes the channel vector corresponding to the k -th subcarrier.

Fig. 1 presents a comparison of angular-delay domain CSI samples between business and rural areas. The CSI samples are simulated using the QuaDRiGa toolbox [23] and visualized in grayscale. It can be observed that rural-area CSI exhibits sparsity due to the presence of fewer multipath clusters, while the CSI from the business area demonstrates richer features with larger angular and delay spreads, resulting from the dense scattering environment.

Next, we analyze the impact of UE speed v , which primarily influences the temporal variation of the wireless channel. To clearly demonstrate this effect, Fig. 1 presents a comparison of

channel samples corresponding to low and high UE mobility, specifically at speeds of $v = 24$ km/h and $v = 300$ km/h, respectively. The associated frequency-time domain channels, denoted by $\mathbf{H}_{\text{cplx},m,n}$, are visualized as grayscale CSI maps. As observed, the CSI map corresponding to low mobility exhibits stable features along the time axis, whereas the high-mobility case results in significant temporal variations, reflecting the dynamic nature of the underlying channel conditions.

In summary, the conditioning information that characterizes the channel can be represented by the label vector $\mathbf{c} = [x, y, v]$, which encodes the UE's location and speed. Let $\mathbf{H} \in \mathbb{R}^{N_r \times \tau \times S \times 2}$ denote the real-valued channel tensor obtained by applying a 2D-FFT to the complex-valued channel \mathbf{H}_{cplx} , followed by a concatenation of its real and imaginary components along the last dimension. For notational convenience in the proposed DM-based framework (to be detailed in Sec. III), the tensor \mathbf{H} is further vectorized into a one-dimensional representation denoted by \mathbf{h} . The relationship between the channel representation \mathbf{h} and the conditioning label \mathbf{c} gives rise to a conditional channel distribution denoted by $q(\mathbf{h}|\mathbf{c})$. To address the issue of limited availability of measured channel data, as discussed in the previous subsection, and to support downstream tasks such as receiver processing, this work aims to learn an approximate conditional distribution $\hat{q}(\mathbf{h}|\mathbf{c})$ that closely matches the true distribution. To achieve this, a conditional DM is developed, as described in Sec. III. Once trained, the conditional DM can be used to generate synthetic channel samples according to $\hat{\mathbf{h}}_{\text{gen}} \sim \hat{q}(\mathbf{h}|\mathbf{c})$, which enables the construction of augmented channel datasets tailored to specific environmental conditions defined by the label \mathbf{c} .

III. PROPOSED APPROACH

A. Main Framework

The overall framework of the proposed approach includes the following steps:

- 1) **Channel Measurements:** Collect a set of N_{train} training samples, consisting of UE location and speed labels $\mathcal{C}_{\text{train}} = \{\mathbf{c}_{\text{train}}^{[j]}\}_{j=1}^{N_{\text{train}}}$ and their corresponding channels $\mathcal{H}_{\text{train}} = \{\mathbf{h}_{\text{train}}^{[j]}\}_{j=1}^{N_{\text{train}}}$. The UE's location-speed labels can be conveyed to the BS via a control link. Channel samples are either obtained in measurement campaigns or produced using a channel simulator. In this paper, we consider the latter and adopt the QuaDRiGa toolbox [23] for channel simulation. To reflect practical limitations, only a limited number of samples are assumed to be available for training.

- 2) **DM Training:** The DM is trained using $\mathcal{H}_{\text{train}}$ by applying a forward diffusion process and learning to reverse it (denoising) while adopting $\mathcal{C}_{\text{train}}$ as the conditional input. The model architecture and training details are provided in Sec. III-B.
- 3) **Scenario-Specific Channel Generation:** Once trained, the DM is used to generate the channel dataset $\mathcal{H}_{\text{gen}} = \{\hat{\mathbf{h}}_{\text{gen}}^{[j]}\}_{j=1}^{N_{\text{gen}}}$ given new sets of location-speed labels $\mathcal{C}_{\text{gen}} = \{\mathbf{c}_{\text{gen}}^{[j]}\}_{j=1}^{N_{\text{gen}}}$ tailored to the scenarios intended for enhancement.
- 4) **Neural Receiver Training with Augmented Dataset:** The final stage involves constructing a training dataset for the neural receiver using the augmented channel dataset $\mathcal{H}_{\text{train}} \cup \mathcal{H}_{\text{gen}}$. The detailed construction is presented in Sec. III-C.

B. Scenario-Specific Channel Generation

1) *DM-Based Conditional Generation:* DMs are one of the most advanced generative models, which construct a Markovian process that incrementally adds noise to diffuse structured data $\mathbf{h} \sim q_{\text{data}}(\cdot)$ and learn a reverse process that generates data from noise by denoising [20], [24]. We begin with the basic notations in these processes. The noisy latent variables within the forward diffusion process are represented as $\{\tilde{\mathbf{h}}_t\}_{t \in [0, T]}$, where t denotes the time variable, and T is a fixed constant representing the time range. Let $q_t(\cdot)$ denote the distribution of $\tilde{\mathbf{h}}_t$. The initial distribution of the forward diffusion process is given by $q_0(\cdot) = q_{\text{data}}(\cdot)$, and the final distribution $q_T(\cdot)$ is an isotropic Gaussian. The noise added in the forward diffusion process at time t is denoted as ϵ_t , which is approximated using a noise prediction NN $\epsilon_{\theta}(\tilde{\mathbf{h}}_t, t)$ parameterized by θ in the reverse process for denoising and generation.

The diffusion process can be represented as a stochastic differential equation (SDE) given by

$$d\tilde{\mathbf{h}}_t = \boldsymbol{\mu}(\tilde{\mathbf{h}}_t, t)dt + g(t)d\mathbf{w}_t, \quad (4)$$

where $\boldsymbol{\mu}(\cdot, \cdot)$ and $g(\cdot)$ denote the drift and diffusion coefficients, respectively, and \mathbf{w}_t is a standard Brownian process. A distinct feature of this SDE is that it possesses a probability-flow ordinary differential equation (PF-ODE) as the reverse process, whose solution trajectory distribution at time t aligns with the marginal distribution $q_t(\cdot)$:

$$d\hat{\mathbf{h}}_t = \left[\boldsymbol{\mu}(\hat{\mathbf{h}}_t, t) - \frac{1}{2}g^2(t)\nabla_{\hat{\mathbf{h}}} \log q_t(\hat{\mathbf{h}}_t) \right] dt, \quad (5)$$

where $\{\hat{\mathbf{h}}_t\}_{t \in [0, T]}$ denotes the denoised channel variables within the reverse diffusion process, and $\nabla_{\hat{\mathbf{h}}} \log q_t(\hat{\mathbf{h}}_t)$ represents the score function of $q_t(\hat{\mathbf{h}}_t)$, pointing to the high-density region of data.

In alignment with established practices presented in [25], we set $\boldsymbol{\mu}(\hat{\mathbf{h}}_t, t) = \mathbf{0}$ and $g(t) = \sqrt{2t}$ in this work. Under this configuration, the noise schedule in the diffusion process becomes $\sigma(t) = t$, leading to the conditional distribution of the noisy latent variable $\tilde{\mathbf{h}}_t$ being expressed as $q(\tilde{\mathbf{h}}_t|\mathbf{h}) = \mathcal{N}(\tilde{\mathbf{h}}_t; \mathbf{h}, t^2\mathbf{I})$ [24]–[26]. To numerically solve the PF-ODE, the time range $t \in [0, T]$ is split into a series of time intervals with $(N + 1)$ boundaries, denoted as $\epsilon = t_0 < \dots < t_N = T$. Herein, ϵ is a predefined small positive constant introduced to avoid numerical instability. Specifically, we follow [25] to set $t_0 = \epsilon = 0.002$, $t_N = T = 80$, and

$$t_n = \left(t_0^{1/\omega} + \frac{n}{N} (t_N^{1/\omega} - t_0^{1/\omega}) \right)^\omega \quad (6)$$

with $\omega = 7$.

To enable the reverse process for sample generation, we should further have an approximation of the score function $\nabla_{\hat{\mathbf{h}}} \log q_t(\hat{\mathbf{h}}_t)$. This approximation can be achieved by denoising score matching [27], which leverages a denoiser $\mathbf{d}_\theta(\mathbf{h}_t, t)$ to estimate the score:

$$\nabla_{\hat{\mathbf{h}}} \log q_t(\hat{\mathbf{h}}_t) \approx \frac{\mathbf{d}_\theta(\hat{\mathbf{h}}_t, t) - \hat{\mathbf{h}}_t}{t^2}. \quad (7)$$

The denoiser is optimized by minimizing the expectation of the l_2 denoising error $\|\mathbf{d}_\theta(\hat{\mathbf{h}}_t, t) - \mathbf{h}\|_2^2$ for samples \mathbf{h} drawn from $q_{\text{data}}(\cdot)$.

Given the above configurations and approximation, an empirical estimate of the PF-ODE for sampling can be expressed as

$$\frac{d\hat{\mathbf{h}}_t}{dt} = \frac{\hat{\mathbf{h}}_t - \mathbf{d}_\theta(\hat{\mathbf{h}}_t, t)}{t}. \quad (8)$$

This empirical PF-ODE can be solved using the Euler [24] or Heun [25] numerical ODE solvers, providing the sampling trajectory from $\hat{\mathbf{h}}_T \sim \mathcal{N}(\mathbf{0}, T^2\mathbf{I})$ to $\hat{\mathbf{h}}_\epsilon$. The final estimate $\hat{\mathbf{h}}_\epsilon$ converges to an approximate sample from the target data distribution $q_{\text{data}}(\cdot)$.

In our proposed approach, a DM is employed to generate channel tensors \mathbf{h} conditioned on the UE location-speed vector \mathbf{c} , thereby capturing environment-specific characteristics through conditional generation. Specifically, \mathbf{c} serves as the conditional input that guides the reverse diffusion process, represented as $q_\theta(\hat{\mathbf{h}}_{t_{n-1}}|\hat{\mathbf{h}}_{t_n}, \mathbf{c})$. To incorporate this conditional dependency, the denoiser \mathbf{d}_θ is designed to accept \mathbf{c} as a conditional input, denoted as $\mathbf{d}_\theta(\cdot, \cdot; \mathbf{c})$. Furthermore, to enhance training stability, we construct the denoiser using a preconditioned architecture that integrates a skip connection and the noise prediction model $\boldsymbol{\epsilon}_\theta$ as

$$\mathbf{d}_\theta(\hat{\mathbf{h}}_t, t; \mathbf{c}) = c_{\text{skip}}(t)\hat{\mathbf{h}}_t + c_{\text{out}}(t)\boldsymbol{\epsilon}_\theta(\hat{\mathbf{h}}_t, t; \mathbf{c}), \quad (9)$$

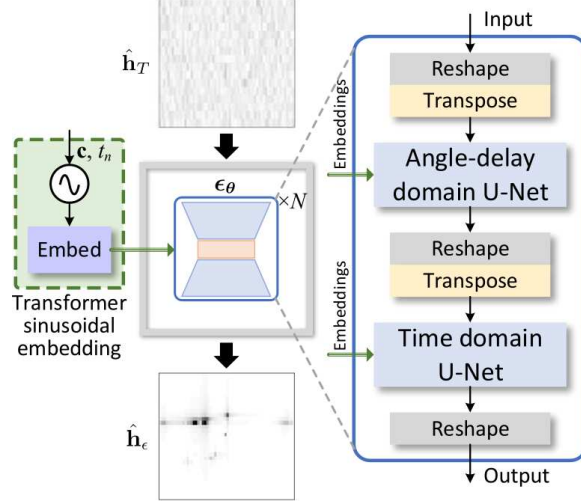


Fig. 2. Conditional generation process using the NN ϵ_θ . The channel samples $\hat{\mathbf{h}}_T$ and $\hat{\mathbf{h}}_\epsilon$ are illustrated as 2D grayscale images for clarity.

where $c_{\text{skip}}(t)$ is used to modulate the skip connection, and $c_{\text{out}}(t)$ scales the noise prediction model's output. The selection of these two functions is given by

$$c_{\text{skip}}(t) = \frac{\sigma_d^2}{\sigma_d^2 + (t - \epsilon)^2}, \quad c_{\text{out}}(t) = \frac{(t - \epsilon) \cdot \sigma_d}{\sqrt{\sigma_d^2 + t^2}}, \quad (10)$$

where σ_d is empirically set to 0.5 based on a parameter scan over the range $[0.1, 1.0]$. This value achieves a trade-off between gradient stability and convergence speed, thereby balancing the two weighting coefficients and ensuring stable training. This configuration ensures that the output of ϵ_θ maintains unit variance, which effectively stabilizes gradient magnitudes during training regardless of varying noise levels. Consequently, the final distribution of the constructed reverse process provides an accurate approximation of the true conditional channel distribution $q(\mathbf{h}|\mathbf{c})$, facilitating scenario-aware channel sample generation.

Given the denoising score matching approximation in (7), the objective function of learning the reverse process can be written as [27]

$$\mathcal{L}_\theta = \mathbb{E}_{\mathbf{h}, \hat{\mathbf{h}}_{t_n}, n} \left[\|\mathbf{d}_\theta(\hat{\mathbf{h}}_{t_n}, t_n; \mathbf{c}) - \mathbf{h}\|_2^2 \right], \quad (11)$$

where $\mathbf{h} \sim q_{\text{data}}(\cdot)$, $\hat{\mathbf{h}}_{t_n} \sim \mathcal{N}(\mathbf{h}, t_n^2 \mathbf{I})$, and $n \sim \mathcal{U}(\{1, \dots, N\})$. Considering the relationship between the denoiser and the noise prediction model ϵ_θ , this objective can be equivalently reformulated as minimizing the error between the predicted noise $\epsilon_\theta(\hat{\mathbf{h}}_{t_n}, t_n; \mathbf{c})$ and the true noise ϵ_{t_n} injected by the forward SDE at any time t_n ($n = 1, \dots, N$).

Algorithm 1 DM-Based Conditional Generation

Input: $\epsilon_\theta(\cdot, \cdot; \cdot)$, $c_{\text{skip}}(t)$, $c_{\text{out}}(t)$, $t_n \in \{0, \dots, N\}$, \mathcal{C}_{gen} .

- 1: **Initialize:** $\hat{\mathbf{h}}_{t_N} = \hat{\mathbf{h}}_T \sim \mathcal{N}(\mathbf{0}, T^2 \mathbf{I})$, $\mathbf{c} \sim \mathcal{C}_{\text{gen}}$.
- 2: **for** $n = N$ to 1 **do**
- 3: Compute $\mathbf{d}_\theta(\hat{\mathbf{h}}_{t_n}, t_n; \mathbf{c})$ using (9).
- 4: $\mathbf{d}_n \leftarrow \frac{\hat{\mathbf{h}}_{t_n} - \mathbf{d}_\theta(\hat{\mathbf{h}}_{t_n}, t_n; \mathbf{c})}{t_n}$.
- 5: $\hat{\mathbf{h}}'_{t_{n-1}} \leftarrow \hat{\mathbf{h}}_{t_n} + (t_{n-1} - t_n) \mathbf{d}_n$.
- 6: Compute $\mathbf{d}_\theta(\hat{\mathbf{h}}'_{t_{n-1}}, t_{n-1}; \mathbf{c})$ using (9).
- 7: $\mathbf{d}'_n \leftarrow \frac{\hat{\mathbf{h}}'_{t_{n-1}} - \mathbf{d}_\theta(\hat{\mathbf{h}}'_{t_{n-1}}, t_{n-1}; \mathbf{c})}{t_{n-1}}$.
- 8: $\hat{\mathbf{h}}_{t_{n-1}} \leftarrow \hat{\mathbf{h}}_{t_n} + (t_{n-1} - t_n) (\frac{1}{2} \mathbf{d}_n + \frac{1}{2} \mathbf{d}'_n)$.
- 9: **end for**

Output: $\hat{\mathbf{h}}_\epsilon = \hat{\mathbf{h}}_{t_0}$.

The conditional generation process is presented in Fig. 2, which produces a synthetic channel sample $\hat{\mathbf{h}}_\epsilon$ from the pure Gaussian noise $\hat{\mathbf{h}}_T$ given \mathbf{c} and t through N iterations of the ODE solver with $t = t_1, \dots, t_N$. At iteration n , the network outputs the estimated noise $\epsilon_\theta(\hat{\mathbf{h}}_{t_n}, t_n; \mathbf{c})$, which is utilized to construct $\hat{\mathbf{h}}_{t_{n-1}}$ based on the ODE solver. We adopt the Heun solver in our implementation. Details of the sampling algorithm are summarized in Algorithm 1 and clarified in the Appendix. Each generated $\hat{\mathbf{h}}_\epsilon$ is collected as $\hat{\mathbf{h}}_{\text{gen}}^{[j]}$ to constitute \mathcal{H}_{gen} for the subsequent augmentation.

Fig. 2 also illustrates the architectural design of ϵ_θ . To effectively generate 3D CSI samples that align with the true channel statistics, the NN architecture is customized beyond conventional designs that utilize a standard U-Net structure [28]. The proposed architecture consists of two cascaded subnetworks, denoted as ϵ'_{θ_1} and ϵ'_{θ_2} , each adopting the U-Net structure as its backbone. Since a standard U-Net operates on two-dimensional data, the input tensor $\hat{\mathbf{h}}_t$ is reshaped and permuted into two formats: $BS \times N_r \times \tau \times 2$ and $B \times N_r \tau \times S \times 2$, where B denotes the batch size. These two representations are then fed into ϵ'_{θ_1} and ϵ'_{θ_2} , respectively.

The first subnetwork focuses on extracting spatial features in the angular-delay domain, while the second captures temporal variations across consecutive symbols. Although both subnetworks share the same architectural configuration, they are trained with independent parameter sets, θ_1 and θ_2 , to specialize in their respective domains. This architecture extends the applicability of

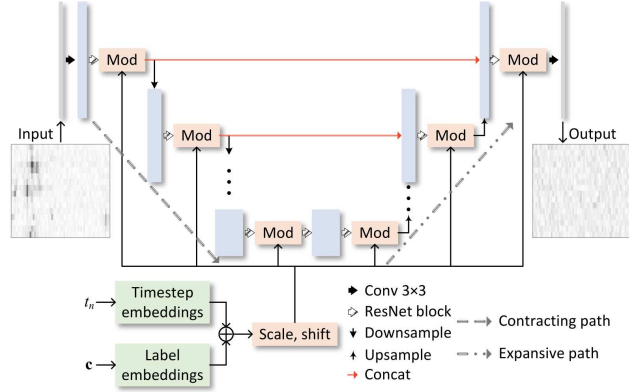


Fig. 3. U-Net architecture of the subnetwork.

diffusion models from conventional two-dimensional data to the generation of three-dimensional channel tensors by jointly modeling spatial and temporal characteristics. To enable conditional generation, the conditioning label c , along with the diffusion time step t_n , is incorporated into the network via Transformer-style sinusoidal positional encoding [29], followed by a dense embedding layer.

The architecture of the U-Net used in the subnetworks is illustrated in Fig. 3. It consists of a contracting path and an expansive path across multiple resolution levels. The contracting path is designed to extract multi-scale features from the input through a sequence of residual blocks based on the ResNet architecture [30]. Each block includes convolutional layers, activation functions, and residual connections. To enhance spatial feature learning, self-attention modules are inserted at selected downsampling stages. The expansive path reconstructs the noise prediction output from the intermediate features using a sequence of residual blocks, each followed by an upsampling layer that doubles the resolution of the feature map. This structure enables the recovery of fine-grained spatial information from compressed feature representations. To enable conditional generation, the timestep and scenario label c are embedded and transformed into scale and shift vectors. These vectors modulate the activations within the ResNet blocks, allowing the network to adapt to different channel conditions.

2) *Consistency Distillation for Acceleration:* A major limitation of DM-based generation is the slow inference speed, as the process typically requires N iterative steps, often in the order of hundreds. This subsection introduces a scheme that significantly reduces the number of required steps while preserving generation quality.

To accelerate generation, we utilize the consistency distillation strategy [31] to achieve one-step generation without significantly compromising the quality. This strategy aims at constructing a consistency model (CM) that can map any latent variables $\hat{\mathbf{h}}_t$ on the same trajectory to a consistent origin $\hat{\mathbf{h}}_\epsilon$. Specifically, this property can be represented by a consistency function \mathbf{f}_θ satisfying

$$\mathbf{f}_\theta(\hat{\mathbf{h}}_t, t; \mathbf{c}) = \mathbf{f}_\theta(\hat{\mathbf{h}}_{t'}, t'; \mathbf{c}), \quad \forall t, t' \in [\epsilon, T]. \quad (12)$$

With this property, one-step generation to synthesize the target data can be achieved through $\hat{\mathbf{h}}_\epsilon = \mathbf{f}_\theta(\hat{\mathbf{h}}_T, T; \mathbf{c})$.

We derive the CM by distilling the denoiser \mathbf{d}_θ in the teacher DM trained in the previous subsection. A notable reason for choosing \mathbf{d}_θ as the teacher is that its parameterization in (9) and (10) naturally satisfies the boundary condition $\mathbf{f}_\theta(\hat{\mathbf{h}}_\epsilon, \epsilon; \mathbf{c}) = \hat{\mathbf{h}}_\epsilon$ implied by (12) since $c_{\text{skip}}(\epsilon) = 1$ and $c_{\text{out}}(\epsilon) = 0$. The distillation can be achieved by minimizing the following objective

$$\begin{aligned} & \mathcal{L}(\boldsymbol{\theta}, \boldsymbol{\theta}^-) \\ &= \mathbb{E}[\|\mathbf{f}_\theta(\hat{\mathbf{h}}_{t_{n+1}}, t_{n+1}; \mathbf{c}) - \mathbf{f}_{\boldsymbol{\theta}^-}(\hat{\mathbf{h}}_{t_n}^\Phi, t_n; \mathbf{c})\|_2^2], \end{aligned} \quad (13)$$

where the expectation is taken over $\mathbf{h} \sim q_{\text{data}}(\cdot)$, $n \sim \mathcal{U}(\{0, \dots, N-1\})$, and $\hat{\mathbf{h}}_{t_{n+1}} \sim \mathcal{N}(\mathbf{h}, t_{n+1}^2 \mathbf{I})$. $\boldsymbol{\theta}^-$ is a running average of the preceding values of $\boldsymbol{\theta}$ during the course of training [31]. $\hat{\mathbf{h}}_{t_n}^\Phi$ is an estimate of $\hat{\mathbf{h}}_{t_n}$ from $\hat{\mathbf{h}}_{t_{n+1}}$ by adopting one step of the numerical ODE solver Φ , given by

$$\hat{\mathbf{h}}_{t_n}^\Phi = \hat{\mathbf{h}}_{t_{n+1}} + (t_n - t_{n+1})\Phi(\hat{\mathbf{h}}_{t_{n+1}}, t_{n+1}). \quad (14)$$

Similar to the DM-based sampling elucidated in Sec. III-B1, the Heun solver is utilized, and the update rules of the corresponding Φ can be found in Algorithm 1.

The parameters $\boldsymbol{\theta}$ are updated based on gradient descent over (13) with a learning rate $\eta = 10^{-5}$, while $\boldsymbol{\theta}^-$ is refined after each gradient descent step using exponential moving average:

$$\boldsymbol{\theta}^- = \text{stopgrad}(\beta \boldsymbol{\theta}^- + (1 - \beta) \boldsymbol{\theta}), \quad (15)$$

where the operation $\text{stopgrad}(\cdot)$ blocks the gradient propagation to enhance the stability in training, and β denotes the decay rate, which is empirically chosen as 0.95 in this work.

The training procedure of consistency distillation is outlined in Algorithm 2. As $\boldsymbol{\theta}^-$ represents an average of $\boldsymbol{\theta}$ during training, these parameters converge to identical values ($\boldsymbol{\theta}^- = \boldsymbol{\theta}$) upon reaching equilibrium. Once trained, the distilled CM can produce target samples $\hat{\mathbf{h}}_\epsilon$ from Gaussian-distributed inputs $\hat{\mathbf{h}}_T$ at time T through the deterministic mapping $\hat{\mathbf{h}}_\epsilon = \mathbf{f}_\theta(\hat{\mathbf{h}}_T, T; \mathbf{c})$.

Algorithm 2 Consistency Distillation

Input: $\mathcal{H}_{\text{train}}, \mathcal{C}_{\text{train}}, \eta, \beta, \Phi(\cdot, \cdot)$, initial model parameter θ .

- 1: **Initialize:** $\theta^- \leftarrow \theta; \hat{\mathbf{h}}_T \sim \mathcal{N}(\mathbf{0}, T^2 \mathbf{I})$.
- 2: **repeat**
- 3: Sample $\mathbf{h} \sim \mathcal{H}_{\text{train}}, \mathbf{c} \sim \mathcal{C}_{\text{train}}$ and $n \sim \mathcal{U}(\{0, \dots, N-1\})$.
- 4: Sample $\hat{\mathbf{h}}_{t_{n+1}} \sim \mathcal{N}(\mathbf{h}, t_{n+1}^2 \mathbf{I})$.
- 5: Compute $\hat{\mathbf{h}}_{t_n}^\Phi$ using (14).
- 6: Compute $\mathcal{L}(\theta, \theta^-) \leftarrow \|\mathbf{f}_\theta(\hat{\mathbf{h}}_{t_{n+1}}, t_{n+1}; \mathbf{c}) - \mathbf{f}_{\theta^-}(\hat{\mathbf{h}}_{t_n}^\Phi, t_n; \mathbf{c})\|_2^2$.
- 7: Compute $\theta \leftarrow \theta - \eta \nabla_\theta \mathcal{L}(\theta, \theta^-)$.
- 8: Compute $\theta^- \leftarrow \text{stopgrad}(\beta \theta^- + (1 - \beta) \theta)$.
- 9: **until** convergence

Output: Distilled CM $\mathbf{f}_\theta(\cdot, \cdot)$.

C. Data Augmentation for the SIP Neural Receiver

We adopt the neural receiver proposed in [6] for SIP transmission. The neural receiver contains two ResNet-based NNs targeted channel estimation and data detection, respectively, and adopts the interference cancellation scheme to enhance accuracy.

The input-output relationship of the neural receiver function R , which involves I interference cancellation iterations between the channel estimator and the data detector, is given by

$$\hat{\mathbf{B}}_i, \hat{\mathbf{H}}_{\text{SF},i} = R(\mathbf{Y}, \mathbf{P}), \quad 1 \leq i \leq I, \quad (16)$$

where $\mathbf{Y} \in \mathbb{R}^{N_r \times K \times S \times 2}$ and $\mathbf{P} \in \mathbb{R}^{N_t \times K \times S \times 2}$ represent the real-valued received signal tensor and pilot tensor, respectively. $\hat{\mathbf{B}}_i \in \mathbb{R}^{N_t \times K \times S \times Q}$ and $\hat{\mathbf{H}}_{\text{SF},i} \in \mathbb{R}^{N_r \times N_t \times K \times S \times 2}$ denote the (soft) estimated bits and the estimated channel in the spatial-frequency domain, respectively, where Q is the number of bits per symbol corresponding to the quadrature amplitude modulation (QAM) order. The training objective of the neural receiver can be written as

$$\min_{\Theta} \frac{1}{I} \sum_{i=1}^I \left\{ \mathcal{L}_{\text{BCE}}(\mathbf{B}, \hat{\mathbf{B}}_i) + \mathcal{L}_{\text{MSE}}(\mathbf{H}_{\text{SF}}, \hat{\mathbf{H}}_{\text{SF},i}) \right\}, \quad (17)$$

where Θ is the parameter set of the neural receiver. \mathcal{L}_{BCE} and \mathcal{L}_{MSE} denote the binary cross entropy (BCE) and mean square error (MSE) loss. \mathbf{B} and \mathbf{H}_{SF} are the encoded bits and the true channel in the spatial-frequency domain.

TABLE I
PARAMETER SETTINGS IN THE CHANNEL SIMULATION

Antenna setting	BS: $N_r = 32$ ULA antennas UE: single antenna ($N_t = 1$)
Center frequency	2.655 GHz
Bandwidth	10 MHz
FFT size (subcarriers)	$K = 512$
OFDM symbol number	$S = 14$
Delay domain length	$\tau = 32$
Subregion range	20 m \times 20 m
UE speed	24 km/h, 300 km/h
Pre-augmentation channel samples	1000 (200 samples per subregion) Evenly split between 24 km/h and 300 km/h

TABLE II
DESCRIPTIONS OF DIFFERENT SUBREGIONS

Subregion	Center position[m]	Scenario	Clusters
R1 business area	(50, 0)	3GPP-38.901-UMi-NLOS	40
R2 residential area	(-100, -50)	3GPP-38.901-UMi-NLOS	40
R3 rural area	(10, -70)	3GPP-38.901-UMi-LOS	5
R4 parking lot	(90, -160)	3GPP-38.901-UMi-LOS	5
R5 warehouse	(0, 170)	3GPP-38.901-UMi-NLOS	10

The augmented dataset for training the neural receiver can be divided into pairs of the form $\{\mathbf{Y}^{[j]}, \mathbf{P}^{[j]}, \mathbf{B}^{[j]}, \mathbf{H}_{\text{SF}}^{[j]}\}$. To construct this dataset, the channel tensors within $\mathcal{H}_{\text{train}} \cup \mathcal{H}_{\text{gen}}$ are first transformed into the spatial-frequency domain to obtain $\mathbf{H}_{\text{SF}}^{[j]}$ using a 2D-inverse FFT. Subsequently, the pilot tensor $\mathbf{P}^{[j]}$ and bit tensor $\mathbf{B}^{[j]}$ are randomly generated. The corresponding received signal tensor $\mathbf{Y}^{[j]}$ is then derived based on (3), with SNRs randomly selected from a predefined range.

IV. NUMERICAL RESULTS

A. Simulation Setups

We utilize the QuaDRiGa software tool [23] to simulate the wireless channels. The simulation parameter settings are summarized in Table I. Following the setup in [22], five representative subregions are modeled within an urban microcell (UMi) environment, as detailed in Table II.

TABLE III
HYPERPARAMETERS OF EACH U-NET SUBNETWORK

Hyperparameter	Channel dim.	Multipliers	#ResNet blocks	#Params
Value	128	{1, 2, 3, 4}	1	72.43M

Note: Channel dim. denotes the depth of the first convolutional layer.
Multipliers are applied to the depth of subsequent resolution levels.

Each subregion is a square area measuring 20 m by 20 m, centered at the specified coordinates. The BS is located at the origin (0, 0), and UEs are uniformly distributed within the subregions and follow linear movement trajectories. A training dataset consisting of 1000 channel samples ($N_{\text{train}} = 1000$) is used to train the generative models prior to channel synthesis and augmentation. Specifically, 200 samples are generated per subregion, with an equal division between UEs moving at 24 km/h and 300 km/h.

The U-Net architectures used in both the DM and the CM have an initial convolutional depth of 128. The depth multipliers across the four resolution levels are set to 1, 2, 3, 4, and each resolution level includes one ResNet block. The detailed hyperparameters of each U-Net subnetwork are summarized in Table III. The diffusion process uses $N = 40$ steps, and both DM and CM are trained for 800 epochs.

For the SIP scheme, the power allocation factor is selected as $\rho = 0.3$. Pilot symbols are modulated using quadrature phase shift keying (QPSK), while data symbols employ 16-QAM. Low-density parity-check (LDPC) codes with a code rate of $r = 490/1024$ are utilized. In the neural receiver, the number of interference cancellation iterations is set to $I = 2$, and both the channel estimation and data detection modules use six ResNet blocks. The receiver is trained for 300 epochs using the Adam optimizer with an initial learning rate of 0.001. During training, the SNR values are randomly selected within the range of $[-5, 0]$ dB. As a baseline, we include a conventional OP scheme using N_p pilot symbols, with linear minimum MSE (LMMSE)-based channel estimation and data detection. To evaluate performance, the block error rate (BLER) is computed over 10,000 transmitted frames. The throughput is then calculated based on the BLER using the following equation:

$$\text{Throughput} = K \times S \times \Omega \times Q \times r \times (1 - \text{BLER}), \quad (18)$$

where Ω represents the ratio of REs allocated for data symbols. Specifically, for the OP receiver,

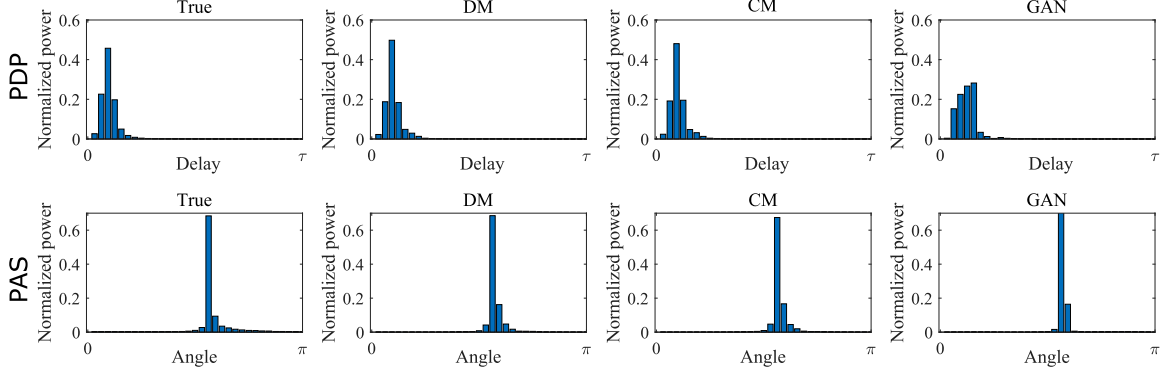


Fig. 4. PDP and PAS of the channel samples from subregion R3.

TABLE IV
WASSERSTEIN-2 DISTANCE BETWEEN THE GENERATED AND
TRUE CHANNEL DATA ACROSS DIFFERENT SUBREGIONS

		R1	R2	R3	R4	R5
AD	DM	1.22e-2	9.86e-3	7.27e-2	6.20e-2	1.07e-2
	CM	1.33e-2	6.92e-3	4.35e-2	3.68e-2	1.45e-2
	GAN	2.16e-1	4.07e-2	2.51e-1	1.08e-1	1.08e-1
FT	DM	1.14e-4	1.50e-4	2.53e-5	1.66e-5	1.23e-4
	CM	1.50e-4	1.45e-4	7.44e-5	5.52e-5	1.17e-4
	GAN	5.83e-4	1.79e-4	1.06e-4	3.25e-4	1.29e-4

Note: “AD” refers to angular-delay domain. “FT” refers to frequency-time domain. The top-performing results are highlighted in **bold**.

$\Omega = (S - N_p)/S$, while for the SIP receiver, $\Omega = 1$.

B. Results and Analysis

1) *Evaluation of Generated Channel Samples:* In this subsection, we evaluate the quality of the channel samples generated by the proposed methods. We begin by comparing the statistical distributions of the true and synthetic channel samples, as illustrated in Fig. 4. For clarity, the comparison focuses on channel samples from subregion R3. As a baseline, we adopt the conditional GAN-based approach from [32]. The power delay profile (PDP) and power angular spectrum (PAS) are calculated by averaging over 5000 channel samples. Fig. 4 demonstrates that the PDP and PAS of the channels generated by the proposed DM and CM closely resemble

TABLE V
KS TEST P-VALUES ACROSS DIFFERENT UE
SPEED

	DM	CM	GAN
24 km/h	2.17e-1	3.02e-1	2.59e-4
300 km/h	2.43e-1	1.42e-1	4.28e-13

Note: The top-performing results are highlighted in **bold**.

those of the true channel samples used to train them. In contrast, the distributions of the samples generated by the GAN approach exhibit significant deviations from the true distribution. These results highlight the superior capability of the proposed methods in accurately modeling channel statistics and generating high-fidelity samples consistent with the underlying scenario.

To provide a quantitative assessment, Table IV presents the Wasserstein-2 distance between the power spectra of the generated and true channel samples. The computation follows the formulation in [14, Eq. (1)]. As shown in the table, the proposed DM- and CM-based approaches yield consistently smaller Wasserstein-2 distances compared to the GAN baseline across all subregions. This holds true in both the antenna-delay and frequency-time domains. These results confirm the superior ability of the proposed methods to align with the true channel distribution and reinforce their effectiveness in high-fidelity channel modeling.

In addition to the Wasserstein-2 distance, we report the Kolmogorov-Smirnov (KS) test p-value to further quantify the distributional similarity between synthetic and true channel samples. A larger p-value indicates that the observed differences can be attributed to random variations, with 0.05 commonly adopted as the significance threshold [33]. Given the multi-dimensional nature of the channel samples, principal component analysis is first applied for dimensionality reduction, after which the KS test is conducted. The results for the frequency-time domain channel samples across different user mobility conditions are presented in Table V. It can be observed that the GAN-based approach yields extremely small p-values, suggesting a clear mismatch with the true distribution. By contrast, the p-values of both the DM and CM exceed the significance level by a large margin, thereby confirming the effective distribution match achieved by these schemes.

Beyond generation quality evaluation, Table VI provides a comparison of DM, CM, and GAN-based approaches in terms of per-sample generation latency, parameter count, and FLOPs. All

TABLE VI
LATENCY, PARAMETERS AND COMPLEXITY COMPARISON

	Latency [ms]	#Params [M]	FLOPs [GFLOPs]
DM	1033	144.86	16615
CM	13	144.86	210.32
GAN	12	156.76	21.13

Note: In the dual U-Net design of the DM/CM's denoising network ϵ_θ , the two subnetworks each account for approximately half of the total parameters and FLOPs. The parameter counts of the GAN's generator and discriminator are 70.31M and 86.45M, respectively.

experiments were conducted on an NVIDIA RTX 4090 GPU to ensure consistency. As shown in the table, the proposed CM achieves a generation speed comparable to that of the GAN-based approach while providing approximately an 80-fold reduction in both sample generation latency and FLOPs compared to the DM method, due to its single-step generation mechanism. Importantly, this acceleration is achieved without compromising generation quality, demonstrating the practical efficiency and effectiveness of the CM architecture. In addition, the parameter counts of the proposed DM and CM remain comparable to those of the GAN. Taken together with their superior generation quality, these results underscore the strong potential of the proposed designs.

2) *Evaluation of Receiver Performance:* To assess the effectiveness of the neural receiver under various channel augmentation strategies, we compare the following methods for constructing the training dataset.

- **True:** Uses ground-truth channel samples corresponding to the target user locations and speeds.
- **GAN:** Augments the limited ground-truth samples with synthetic channel samples generated by a pre-trained conditional GAN.
- **DM (proposed):** Augments the limited ground-truth samples using synthetic channel data generated by a pre-trained conditional DM.
- **CM (proposed):** Augments the limited ground-truth samples using synthetic data generated by a pre-trained conditional CM.
- **Uncond. DM:** Augments the limited ground-truth samples using a pre-trained unconditional DM that does not incorporate scenario-specific conditioning information.

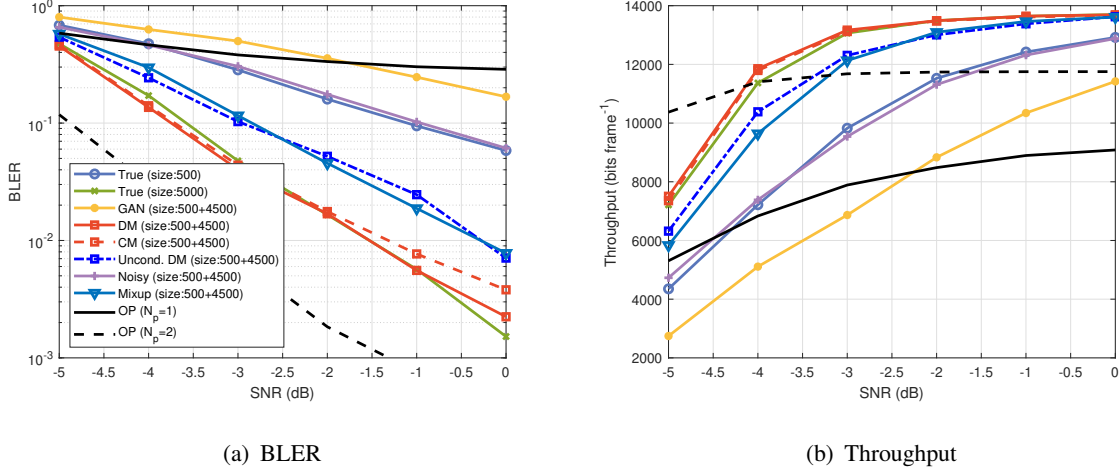


Fig. 5. BLER performance and throughput of various approaches for training the neural receiver when $v = 24$ km/h.

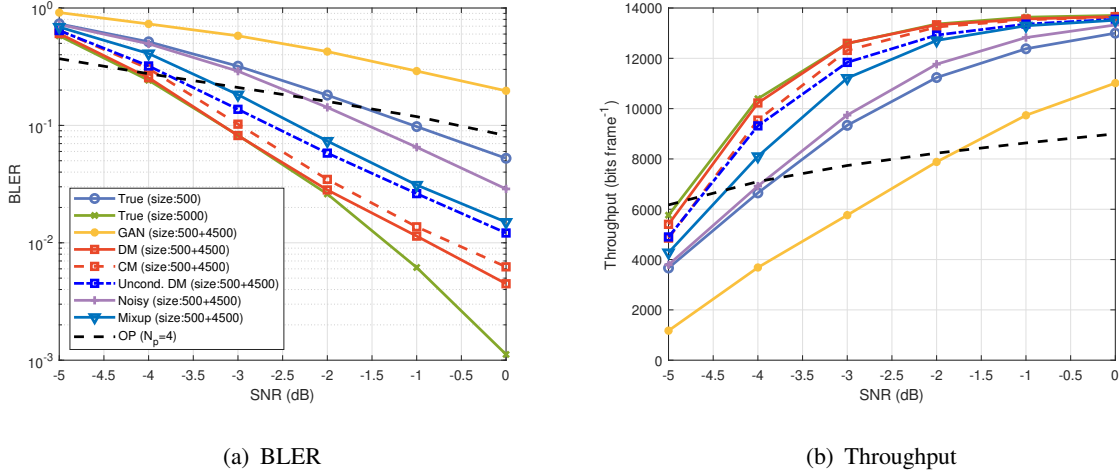


Fig. 6. BLER performance and throughput of various approaches for training the neural receiver when $v = 300$ km/h.

- **Noisy:** Augments the ground-truth samples by adding AWGN to generate synthetic samples.
- **Mixup:** Augments the ground-truth samples by linearly interpolating ground-truth channel tensors $\mathbf{h}_{\text{train}}^{[i]}, \mathbf{h}_{\text{train}}^{[j]}$ randomly drawn from $\mathcal{H}_{\text{train}}$ to generate synthetic samples [34], [35]:

$$\hat{\mathbf{h}} = \lambda \mathbf{h}_{\text{train}}^{[i]} + (1 - \lambda) \mathbf{h}_{\text{train}}^{[j]}, \quad (19)$$

where $\lambda \in [0, 1]$ is a mixing coefficient drawn from a Beta distribution, i.e., $\lambda \sim \text{Beta}(\alpha, \alpha)$, $\alpha > 0$. Following common practice [34], we set $\alpha = 0.4$ in our experiments.

We first evaluate the performance of the SIP receiver under different user mobility conditions, focusing on both BLER and throughput, as depicted in Figs. 5 and 6. Accordingly, the proposed

approaches enable user mobility-aware channel generation and augmentation by conditioning on labels \mathbf{c} containing the corresponding user speed v .

Fig. 5(a) presents the BLER results under a low speed of $v = 24$ km/h. As described in the simulation setup, only a limited number of ground-truth channel samples are available at this speed, specifically $N_{\text{train}}/2 = 500$ samples. To expand the training data, all augmentation methods, namely GAN, DM, CM, and AWGN, generate $N_{\text{gen}} = 4500$ synthetic samples. For performance comparison, we also include a benchmark in which the receiver is trained using 5000 ground-truth channel samples.

As shown in the figure, receivers augmented with DM- and CM-generated samples achieve significant performance gains compared to the receiver trained solely on the limited original dataset. These improvements highlight the effectiveness of the proposed methods in alleviating the issue of data scarcity and enabling scenario-specific channel generation and augmentation. Moreover, the proposed methods perform comparably to the benchmark receiver trained with 5000 real samples and clearly outperform the GAN-, AWGN-, and Mixup-based augmentation. The inferior performance of the GAN-based method can be attributed to the limited diversity of its generated samples, which leads to overfitting during neural receiver training.

In addition, the enhanced SIP receiver exhibits a performance gap of approximately 1.5 to 2 dB compared to the OP receiver with $N_p = 2$. However, as shown in Fig. 5(b), it provides a significant throughput advantage. This improvement results from the efficient use of all transmission resources enabled by the SIP scheme in conjunction with the proposed augmentation strategy.

The BLER performance and throughput shown in Fig. 6(a) and Fig. 6(b) demonstrate that the SIP scheme exhibits much more pronounced gains over the OP transmission under the high-mobility condition with $v = 300$ km/h. The SIP receiver augmented by the proposed approach achieves similar BLER and throughput as those of the receiver trained using 5000 true channel samples, while also outperforming all other baseline methods. Notably, this receiver delivers a throughput improvement of approximately 51.8% over the OP receiver with $N_p = 4$, highlighting the inability of limited pilot resources to track rapid channel variations in highly dynamic environments.

Table VII presents the BLER of the SIP receiver across different subregions. To enable site-specific channel generation and augmentation, the pre-trained conditional DM and CM are employed to generate synthetic samples based on label vectors \mathbf{c} , which encode the corresponding

TABLE VII
BLER PERFORMANCE OF THE SIP RECEIVER ACROSS
DIFFERENT SUBREGIONS ($v = 24$ km/h, SNR = -3 dB)

	R1	R2	R3	R4	R5
True 100 spec.	9.16e-1	7.66e-1	8.90e-2	3.64e-2	4.25e-1
True 1000 spec.	3.19e-2	4.68e-3	<u>3.12e-3</u>	4.76e-3	<u>3.06e-2</u>
DM 1000 spec.	<u>3.38e-2</u>	<u>5.00e-3</u>	3.72e-3	<u>6.64e-3</u>	1.44e-2
CM 1000 spec.	3.90e-2	5.08e-3	2.64e-3	8.88e-3	4.20e-2
True 5000	1.06e-1	1.63e-2	4.04e-3	1.10e-2	8.75e-2
Uncond. DM 5000	2.45e-1	1.72e-2	3.24e-3	1.62e-2	4.41e-2

Note: The top-performing results are highlighted in **bold**, with the second-best results underlined for clarity.

location coordinates. For each subregion, $N_{\text{gen}} = 1000$ synthetic samples are generated and combined with the 100 available ground-truth samples to construct an augmented dataset for training the receiver tailored to that specific subregion. These approaches are denoted as “DM 1000 spec.” and “CM 1000 spec.”, respectively. As performance references, two baselines are considered: “True 100”, which uses only 100 site-specific ground-truth samples, and “True 1000”, which leverages 1000 ground-truth samples generated by QuaDRiGa. Results show that both proposed methods achieve comparable BLER as the “True 1000 spec.” baseline and significantly outperform the “True 100 spec.” baseline across all regions.

In addition, two non-site-specific baselines are included for comparison: (1) “True 5000”, trained on 5000 ground-truth samples drawn from all subregions, and (2) “Uncond. DM 5000”, trained using 5000 synthetic samples generated by an unconditional DM. Since these models are not specialized for individual subregions, they adopt a shared receiver architecture across all subregions. The proposed site-specific methods exhibit substantially lower BLER than both baselines, underscoring the benefit of site-specific augmentation.

3) *Ablation Study and Generalization Analysis:* This subsection presents the ablation study and generalization analysis of the proposed schemes. First, to validate the effectiveness of the proposed dual U-Net architecture, we conduct an ablation study by training a single joint U-Net (with 162.89M parameters), which directly operates on the 2D “image” derived by flattening the angular-delay domain of the 3D CSI. The generated channel samples from this joint U-Net were then used to augment the SIP neural receiver, and the performance was compared with that

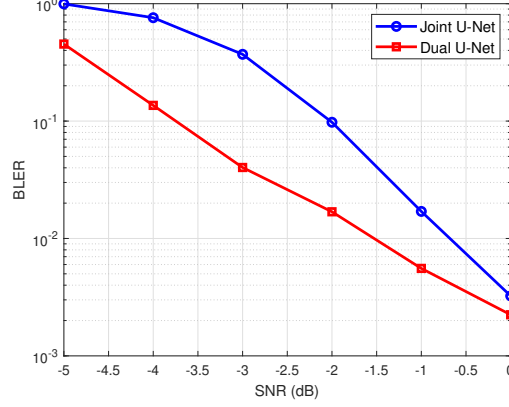


Fig. 7. Ablation study on the proposed dual U-Net architecture: BLER performance comparison between receivers augmented with the joint U-Net-based DM and the dual U-Net-based DM.

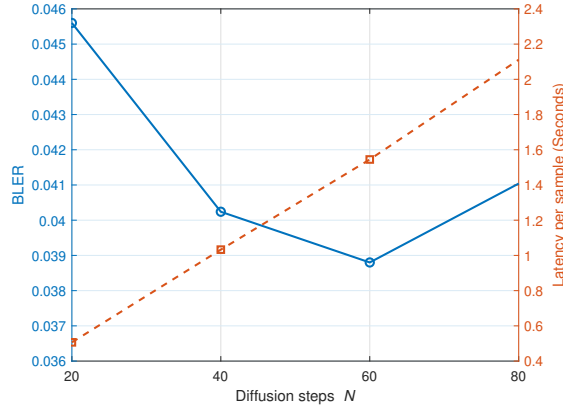


Fig. 8. Ablation study on the proposed DM-based approach's generation latency and BLER with respect to the number of diffusion steps N .

of the receiver augmented by the proposed dual U-Net-based DM. The BLER results under the mobility scenario of $v = 24$ km/h, as presented in Fig. 7, clearly demonstrate that the proposed architecture significantly outperforms the single joint U-Net design, which fails to effectively capture the angular, delay, and temporal CSI features. These results justify our architectural choice.

We then perform an ablation study to evaluate the impact of the diffusion-step parameter N on the BLER performance and generation latency of the proposed DM-based augmentation approach, as presented in Fig. 8. Specifically, BLER is evaluated under $\text{SNR} = -3$ dB and

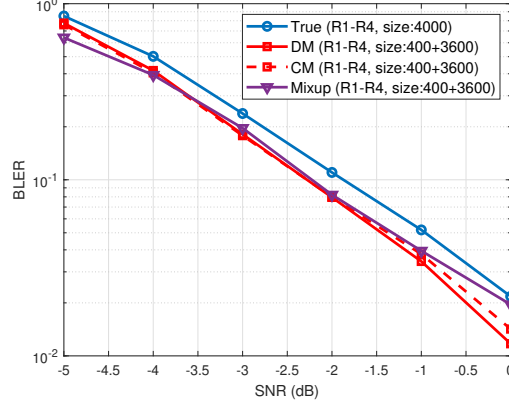


Fig. 9. Generalization study: BLER performance of various approaches for training the neural receiver when $v = 24$ km/h in subregion R5.

$v = 24$ km/h with the augmentation setup of the DM-based approach identical to Fig. 5 of the manuscript, i.e., 500 ground-truth channel samples combined with 4500 synthetic samples for SIP neural receiver training. The results show that the BLER performance remains comparable when $N = 40$, $N = 60$, or $N = 80$, indicating the robustness of the proposed DM-based approach with respect to the choice of N . Considering that the generation latency increases linearly with N , these results substantiate the choice of $N = 40$ as the operating point of the proposed DM-based approach, as it provides a favorable balance between generation quality and efficiency.

Finally, we perform a generalization study of the proposed approach by augmenting the SIP neural receiver with synthetic samples generated for subregions R1-R4 and testing on the unseen subregion R5. The corresponding BLER performance under $v = 24$ km/h is reported in Fig. 9. Specifically, the DM and CM each generate $N_{\text{gen}} = 3600$ synthetic samples for R1-R4 (900 samples per region), which are combined with 400 ground-truth samples to form the augmented training dataset. For comparison, we also include the Mixup baseline and a benchmark receiver trained with 4000 ground-truth samples from R1-R4. As shown in the figure, Mixup, DM, and CM all outperform the benchmark. These results can be attributed to the increased diversity introduced by the synthetic samples, which enhances the generalization capability of the augmentation-based approaches. Furthermore, the proposed DM- and CM-based schemes provide further gains over Mixup, thereby confirming their effectiveness in enhancing robustness to scenario variations.

V. CONCLUSION

This paper proposes a scenario-specific channel generation method based on conditional DMs, designed to enhance neural receiver performance in SIP schemes. The proposed conditional DM is architecturally tailored to capture the complex relationship between channel characteristics and UE location and speed, thereby enabling the generation of high-fidelity channel data aligned with specific deployment environments. To further improve generation efficiency, a consistency distillation technique is introduced, which significantly accelerates the sampling process. The generated synthetic channels effectively address the challenge of data scarcity in training neural receivers. Numerical results demonstrate that the proposed method mitigates the limitations imposed by limited training data and achieves scenario-specific performance that surpasses both general-purpose models trained across multiple scenarios and several existing data augmentation baselines.

APPENDIX

The one-step update rule of the Heun ODE solver, from t_n to t_{n-1} as presented in Algorithm 1, is derived in the following. Define

$$\mathbf{d}_n \triangleq \left. \frac{d\hat{\mathbf{h}}_t}{dt} \right|_{t=t_n} = \frac{\hat{\mathbf{h}}_{t_n} - \mathbf{d}_\theta(\hat{\mathbf{h}}_{t_n}, t_n)}{t_n}, \quad (20)$$

where $n \in \{1, \dots, N\}$. Given Euler's first-order approximation

$$\left. \frac{d\hat{\mathbf{h}}_t}{dt} \right|_{t=t_n} \approx \frac{\hat{\mathbf{h}}_{t_n} - \hat{\mathbf{h}}_{t_{n-1}}}{t_n - t_{n-1}}, \quad (21)$$

we can derive the estimated data point at $t = t_{n-1}$ as

$$\hat{\mathbf{h}}'_{t_{n-1}} \approx \hat{\mathbf{h}}_{t_n} + (t_{n-1} - t_n)\mathbf{d}_n. \quad (22)$$

Nonetheless, it is observed that Heun's second-order method achieves a desirable tradeoff between complexity and truncation error [25]. This method approximates the right-hand side of (21) using the derivative between t_n and t_{n-1} :

$$\begin{aligned} \frac{\hat{\mathbf{h}}_{t_n} - \hat{\mathbf{h}}_{t_{n-1}}}{t_n - t_{n-1}} &\approx \frac{1}{2} \left. \frac{d\hat{\mathbf{h}}_t}{dt} \right|_{t=t_n} + \frac{1}{2} \left. \frac{d\hat{\mathbf{h}}_t}{dt} \right|_{t=t_{n-1}} \\ &= \frac{1}{2}\mathbf{d}_n + \frac{1}{2}\mathbf{d}_{n-1}, \end{aligned} \quad (23)$$

where \mathbf{d}_{n-1} is further approximated using $\hat{\mathbf{h}}'_{t_{n-1}}$ in (22) as

$$\mathbf{d}_{n-1} \approx \mathbf{d}'_n = \frac{\hat{\mathbf{h}}'_{t_{n-1}} - \mathbf{d}_\theta(\hat{\mathbf{h}}'_{t_{n-1}}, t_{n-1})}{t_{n-1}}. \quad (24)$$

Therefore, the estimation of $\hat{\mathbf{h}}_{t_{n-1}}$ can be formulated as

$$\hat{\mathbf{h}}_{t_{n-1}} = \hat{\mathbf{h}}_{t_n} + (t_{n-1} - t_n) \left(\frac{1}{2} \mathbf{d}_n + \frac{1}{2} \mathbf{d}'_n \right), \quad (25)$$

completing the derivation.

REFERENCES

- [1] D. Verenzuela, E. Björnson, and L. Sanguinetti, “Spectral and energy efficiency of superimposed pilots in uplink massive MIMO,” *IEEE Trans. Wireless Commun.*, vol. 17, no. 11, pp. 7099–7115, 2018.
- [2] X. Gan, C. Huang, Z. Yang, C. Zhong, X. Chen, Z. Zhang, Q. Guo, C. Yuen, and M. Debbah, “Bayesian learning for double-RIS aided ISAC systems with superimposed pilots and data,” *IEEE J. Sel. Topics Signal Process.*, vol. 18, no. 5, pp. 766–781, 2024.
- [3] M. Xie, X. Yu, K. Wang, J. Zhang, X. Dang, and C. Yuen, “Superimposed pilots for cell-free massive MIMO over spatial-correlated Rician fading channels,” *IEEE Trans. Wireless Commun.*, vol. 23, no. 12, pp. 19 537–19 552, 2024.
- [4] C. Qian, R. Gu, W. Xu, J. Xu, and X. You, “Enhancing wideband multiuser MIMO uplink using superimposed pilots: Joint receiver design,” *IEEE Wireless Commun. Lett.*, vol. 13, no. 4, pp. 1138–1142, 2024.
- [5] Z. Qin, L. Liang, Z. Wang, S. Jin, X. Tao, W. Tong, and G. Y. Li, “AI empowered wireless communications: From bits to semantics,” *Proc. IEEE*, vol. 112, no. 7, pp. 621–652, 2024.
- [6] H. Xiao, W. Tian, S. Jin, W. Liu, J. Shen, Z. Shi, and Z. Zhang, “Interference cancellation based neural receiver for superimposed pilot in multi-layer transmission,” *China Commun.*, vol. 22, no. 1, pp. 75–88, 2025.
- [7] R. Gu, J. Xu, C. Qian, W. Xu, and R. Xie, “Learning power allocation and channel estimation for superimposed pilot-assisted multiuser MIMO,” *IEEE Wireless Commun. Lett.*, vol. 13, no. 11, pp. 3025–3029, 2024.
- [8] X. Li, X. Zhou, J. Zhang, C.-K. Wen, and S. Jin, “AI-driven iterative receiver for superimposed pilot schemes in MIMO-OFDM systems,” in *IEEE Wireless Commun. Netw. Conf. (WCNC)*, 2025, pp. 1–6.
- [9] F. Ait Aoudia and J. Hoydis, “End-to-end learning for OFDM: From neural receivers to pilotless communication,” *IEEE Trans. Wireless Commun.*, vol. 21, no. 2, pp. 1049–1063, 2021.
- [10] T. Lee, J. Park, H. Kim, and J. G. Andrews, “Generating high dimensional user-specific wireless channels using diffusion models,” *arXiv preprint arXiv:2409.03924*, 2024.
- [11] Z. Wang, J. Zhang, H. Du, D. Niyato, S. Cui, B. Ai, M. Debbah, K. B. Letaief, and H. V. Poor, “A tutorial on extremely large-scale MIMO for 6G: Fundamentals, signal processing, and applications,” *IEEE Commun. Surveys Tuts.*, vol. 26, no. 3, pp. 1560–1605, 2024.
- [12] L. Bariah, Q. Zhao, H. Zou, Y. Tian, F. Bader, and M. Debbah, “Large generative AI models for Telecom: The next big thing?” *IEEE Commun. Mag.*, vol. 62, no. 11, pp. 84–90, 2024.
- [13] H. Xiao, W. Tian, W. Liu, and J. Shen, “ChannelGAN: Deep learning-based channel modeling and generating,” *IEEE Wireless Commun. Lett.*, vol. 11, no. 3, pp. 650–654, 2022.
- [14] U. Sengupta, C. Jao, A. Bernacchia, S. Vakili, and D.-s. Shiu, “Generative diffusion models for radio wireless channel modelling and sampling,” in *IEEE Global Commun. Conf. (GLOBECOM)*, 2023, pp. 4779–4784.

- [15] B. Fesl, M. Baur, F. Strasser, M. Joham, and W. Utschick, "Diffusion-based generative prior for low-complexity MIMO channel estimation," *IEEE Wireless Commun. Lett.*, vol. 13, no. 12, pp. 3493–3497, 2024.
- [16] X. Zhou, L. Liang, J. Zhang, P. Jiang, Y. Li, and S. Jin, "Generative diffusion models for high dimensional channel estimation," *IEEE Trans. Wireless Commun.*, vol. 24, no. 7, pp. 5840–5854, 2025.
- [17] G. Chi, Z. Yang, C. Wu, J. Xu, Y. Gao, Y. Liu, and T. X. Han, "RF-diffusion: Radio signal generation via time-frequency diffusion," in *30th ACM MobiCom*, 2024, pp. 77–92.
- [18] M. Baur, N. Turan, S. Wallner, and W. Utschick, "Evaluation metrics and methods for generative models in the wireless PHY layer," *arXiv preprint arXiv:2408.00634*, 2024.
- [19] J. Sohl-Dickstein, E. Weiss, N. Maheswaranathan, and S. Ganguli, "Deep unsupervised learning using nonequilibrium thermodynamics," in *Int. Conf. Mach. Learn.*, 2015, pp. 2256–2265.
- [20] J. Ho, A. Jain, and P. Abbeel, "Denoising diffusion probabilistic models," *Adv. Neural Inf. Process. Syst.*, vol. 33, pp. 6840–6851, 2020.
- [21] P. Dhariwal and A. Nichol, "Diffusion models beat GANs on image synthesis," *Adv. Neural Inf. Process. Syst.*, vol. 34, pp. 8780–8794, 2021.
- [22] X. Li, J. Guo, C.-K. Wen, S. Jin, S. Han, and X. Wang, "Multi-task learning-based CSI feedback design in multiple scenarios," *IEEE Trans. Commun.*, vol. 71, no. 12, pp. 7039–7055, 2023.
- [23] S. Jaeckel, L. Raschkowski, K. Börner, and L. Thiele, "QuaDRiGa: A 3-D multi-cell channel model with time evolution for enabling virtual field trials," *IEEE Trans. Antennas Propag.*, vol. 62, no. 6, pp. 3242–3256, 2014.
- [24] Y. Song, J. Sohl-Dickstein, D. P. Kingma, A. Kumar, S. Ermon, and B. Poole, "Score-based generative modeling through stochastic differential equations," in *Int. Conf. Learn. Represent.*, 2020.
- [25] T. Karras, M. Aittala, T. Aila, and S. Laine, "Elucidating the design space of diffusion-based generative models," *Adv. Neural Inf. Process. Syst.*, vol. 35, pp. 26 565–26 577, 2022.
- [26] J. Pei, C. Feng, P. Wang, H. Tabassum, and D. Shi, "Latent diffusion model-enabled low-latency semantic communication in the presence of semantic ambiguities and wireless channel noises," *IEEE Trans. Wireless Commun. (Early Access)*, 2025.
- [27] P. Vincent, "A connection between score matching and denoising autoencoders," *Neural Comput.*, vol. 23, no. 7, pp. 1661–1674, 2011.
- [28] O. Ronneberger, P. Fischer, and T. Brox, "U-Net: Convolutional networks for biomedical image segmentation," *arXiv preprint arXiv:1505.04597*, 2015.
- [29] A. Vaswani, N. Shazeer, N. Parmar, J. Uszkoreit, L. Jones, A. N. Gomez, Ł. Kaiser, and I. Polosukhin, "Attention is all you need," *Adv. Neural Inf. Process. Syst.*, vol. 30, 2017.
- [30] K. He, X. Zhang, S. Ren, and J. Sun, "Deep residual learning for image recognition," in *IEEE Conf. Comput. Vis. Pattern Recognit.*, 2016, pp. 770–778.
- [31] Y. Song, P. Dhariwal, M. Chen, and I. Sutskever, "Consistency models," in *Int. Conf. Mach. Learn.*, 2023, pp. 32 211–32 252.
- [32] A. Brock, J. Donahue, and K. Simonyan, "Large scale GAN training for high fidelity natural image synthesis," *arXiv preprint arXiv:1809.11096*, 2018.
- [33] R. L. Wasserstein and N. A. Lazar, "The ASA statement on p-values: context, process, and purpose," pp. 129–133, 2016.
- [34] H. Zhang, M. Cisse, Y. N. Dauphin, and D. Lopez-Paz, "mixup: Beyond empirical risk minimization," *arXiv preprint arXiv:1710.09412*, 2017.
- [35] L. Zhang, Z. Deng, K. Kawaguchi, A. Ghorbani, and J. Zou, "How does mixup help with robustness and generalization?" *arXiv preprint arXiv:2010.04819*, 2020.